Geophysical Journal International

Geophys. J. Int. (2013) doi: 10.1093/gji/ggt400

Geophysical Journal International Advance Access published October 28, 2013

Time-varying autoregressive model for spectral analysis of microseismic experiments and long-period volcanic events

J. B. Tary, R. H. Herrera and M. van der Baan

Department of Physics, University of Alberta, Edmonton, AB T6G 2E1, Canada. E-mail: tary@ualberta.ca

Accepted 2013 September 30. Received 2013 September 17; in original form 2013 March 19

SUMMARY

Recent studies show that the frequency content of continuous passive recordings contains useful information for the study of hydraulic fracturing experiments as well as longstanding applications in volcano and global seismology. The short-time Fourier transform (STFT) is usually used to obtain the time–frequency representation of a seismic trace. Yet, this transform has two main disadvantages, namely its fixed time–frequency resolution and spectral leakage. Here, we describe two methods based on autoregressive (AR) models: the short-time autoregressive method (ST-AR) and the Kalman smoother (KS). These two methods allow for the AR coefficients to vary over time in order to follow time-varying frequency contents. The outcome of AR methods depends mainly on the number of AR coefficients. We use a robust approach to estimate the optimum order of the AR methods that best matches the spectral comparison between Fourier and AR spectra. Comparing the outcomes of the three methods on a synthetic signal, a long-period volcanic event, and microseismic data, we show that the STFT and both AR methods are able to track fast changes in frequency content. The STFT provides reasonable results even for noisy data using a simple and effective algorithm. The coefficients of the AR filter are defined at all time in the case of the KS. However, its better time resolution is slightly offset by a lower frequency resolution and its computational complexity. The ST-AR has a high spectral resolution and the lowest sensitivity to background noises, facilitating the identification of the various frequency components. The estimated AR coefficients can also be used to extract parts of the signal. The study of long-term phenomena, such as resonance frequencies, or transient events, such as long-period events, could help to gain further insight on reservoir deformation during hydraulic fracturing experiments as well as global or volcano seismological signals.

Key words: Time-series analysis; Fourier analysis; Downhole methods; Volcano seismology; Computational seismology.

Downloaded from http://gji.oxfordjournals.org/ at Vienna University Library on April 11, 2014

1 INTRODUCTION

Time–frequency analysis of seismic recordings such as from passive microseismic experiments over geothermal, hydrocarbon or CO_2 sequestration sites or seismological observations from global, regional or volcanological events is important to enhance our understanding on the physical processes associated with (fluid-induced) fracturing and fault rupture. Extraction of unconventional resource like heavy oil relies on the injection of fluids at depth to create fractures and enhance oil recovery. The microseismicity induced by the fracturing of the reservoir is often used to monitor the fluid injection. In the case of low permeability reservoirs, such as tight hydrocarbons, the part of the reservoir where the permeability was increased (i.e. the stimulated rock volume) is then assumed to correspond to the cloud of microseismic events. These events correspond to brittle failure mainly attributed to the reduction in effective stress, with negative magnitudes typically between −3 and −1.

However, the total energy corresponding to the fluid injection is orders of magnitude higher than the brittle failure energy corresponding to the observed microseismicity (Maxwell *et al.* 2008). On the other hand, only the recorded microseismic events are usually included in this calculation. Other kinds of deformations, such as tensile opening or slow slip, must account for a part of the missing energy. Fluid injection monitoring for other applications, such as geothermal operations, carbon capture and storage and waste water disposal, suffers from the same limitation. As the needs in energy are growing and climate change effects are becoming more profound, other approaches are needed to improve our understanding of reservoir deformation.

The time-varying characteristics of the frequency content of continuous, passive microseismic recordings have been shown to contain useful information on the reservoir deformation happening during fracturing experiments (Pettitt *et al.* 2009; Das & Zoback 2011; Tary & van der Baan 2012). Time–frequency representations

© The Authors 2013. Published by Oxford University Press on behalf of The Royal Astronomical Society.

were used by Das & Zoback (2011) to design a bandpass filter adapted to a specific class of unconventional events (long-period long-duration events), while Pettitt *et al.* (2009) show a correlation between a decrease in the amplitude of high-frequency resonances and the migration of the main microseismic activity, that was otherwise not delineated by any microseismic event.

Many sources of resonance frequencies, corresponding to well-defined spectral peaks, have been documented in different contexts such as volcanoes (Chouet 1996), sedimentary basins (Bonnefoy-Claudet *et al.* 2006) or even glaciers (West *et al.* 2010). In volcanoes, glaciers and microseismic experiments, fluids are likely involved in the generation process of some of the resonances. Few potential causes have been suggested, from the repetition of periodic events (Lees *et al.* 2004) and the non-linear flow of incompressible viscous fluid in an irregular channel (Julian 1994), to the resonance of fluid-filled cracks (Aki *et al.* 1977; Chouet 1986). An accurate estimation of the dominant frequency would allow to determine either the interevent periodicity or the physical characteristics of the fluid and associated resonator. Analogies between volcano behaviour and hydraulic fracturing experiments are particularly important. They are both characterized by a family of seismic signals, encompassing short-duration brittle events (volcano-tectonic and microseismic events), long-period (LP) events and resonance frequencies. Examples of causes and interpretations of resonances recorded during microseismic experiments can be found in Tary & van der Baan (2012).

Time–frequency transforms are particularly appropriate for the study of signals with non-stationary frequency contents. The most common transform for time–frequency analysis is the short-time Fourier transform (STFT). This transform takes the fast Fourier transform (FFT) of successive, overlapping windows of a signal. The windows have a fixed length irrespective of the investigated frequencies. The STFT has however two main disadvantages. First, due to the trade-off between time and frequency resolutions, both resolutions are fixed and depend directly on the window size (Reine *et al.* 2009). Time and frequency resolutions can be defined as the ability to distinguish two waveforms and two spectral peaks, respectively. The fixed time–frequency resolution of the STFT implies that in order to obtain a high frequency resolution and identify very close spectral peaks, one will not be able to know accurately the timing of any changes in frequency due to the low time resolution.

Secondly, because methods based on the FFT assume that the signal amplitude is zero outside the observation window (i.e. signal windowing), the spectrum obtained using these methods is characterized by a main lobe with a width proportional to the inverse of the observation window size, and by side-lobe leakage (Harris 1978; Hall 2006). The side-lobes around the main lobe can mask low-amplitude spectral peaks or prevent the distinction between close spectral peaks (Kay & Marple 1981). The choice of an appropriate taper can decrease the side-lobes amplitude, at the expense of decreasing the amplitude and widening the main lobe which decreases the spectral resolution (Hall 2006). Other transforms with variable time–frequency resolution, like the continuous wavelet transform (CWT; Daubechies 1992) and the S-transform (Stockwell *et al.* 1996), can achieve better time–frequency estimates for signals with both low and high frequency contents. They are, however, also displaying spectral smearing due to the finite size of their operator (Hall 2006).

On the other hand, one can use *a priori* information to determine which spectral estimation method is suitable to each specific case. In this study, we are interested in following the time-varying spectra of long-lasting phenomena, such as resonance frequencies or tremor-like signals, characterized by peaked spectra. Autoregressive (AR) models are suitable in this case, because AR filters are infinite impulsive response filters whose poles corresponds to the different modes of a resonator (Lesage *et al.* 2002). AR-based methods, also known as linear prediction filters, are not prone to the limitations of the STFT described in the previous paragraph and are used extensively for the study of resonance frequencies (e.g. Claerbout 1985).

Unlike FFT-based methods, AR methods assume that the signal continues to some extent outside the observation window, improving the spectral resolution and preventing the introduction of side-lobes (Marple 1982). The spectral resolution of AR methods is not directly tied to the time resolution, but depends on the signal-to-noise ratio (SNR) as well as the order of the autoregressive model (Marple 1982; Quirk & Liu 1983). Apart from the accurate estimation of spectral peaks, the decomposition of a signal in a set of AR coefficients allows the reconstruction or the extraction of specific harmonics from the signal. For example, the excitation function of LP events recorded at volcanoes was obtained after deconvolution of the harmonic part of these events (Nakano *et al.* 1998; Lesage *et al.* 2002). The complex frequencies of AR poles can also be used to compute a quality factor which depends on the composition of the fluid filling the resonator (Nakano *et al.* 1998; Kumagai & Chouet 2000).

Hereafter, we first describe the short-time auroregressive (ST-AR) method, an adaptation of the classical Burg method (Burg 1972) for spectral estimation in order to follow time-varying spectra. Then we adapt an AR method developed for biomedical applications by Khan & Dutt (2007). This method, named Kalman smoother (KS), is based on a recursive scheme for the Kalman filter. Both AR methods and the STFT are finally applied to a synthetic signal, a real microseismic data set and a LP event recorded at Misti volcano (Lesage *et al.* 2002), in order to assess their performances on typical problems encountered in seismic data analysis: time and frequency resolutions, noise sensitivity, the ability to track fast frequency variations and their computational cost.

2 METHODS

2.1 Short-time autoregressive method

The ST-AR is a combination of the STFT and autoregressive methods. AR methods are linear prediction filters using the previous samples to predict the following ones (Claerbout 1985). The successive values of a time-series y_n are defined as the weighted sum of the previous p values plus some noise v_n following:

$$y_n = \sum_{k=1}^{p} a^k y_{n-k} + v_n, \tag{1}$$

where n are the time indices, a^k the weighting coefficients of the AR filter, p the number of coefficients also called order of the filter and v_n a white noise with zero mean and variance σ_y^2.

Different techniques exist to find the coefficients of the AR filter a^k from the time-series (Kay & Marple 1981). In order to determine the AR coefficients, we use the Burg method (Burg 1972), which employs a recursive least-squares scheme to estimate the AR coefficients from the reflection coefficients that minimize the prediction errors (e.g. Muthuswamy & Thakor 1998; de Waele & Broersen 2000). The Burg method was preferred to the Yule–Walker method because the latter presents more bias in spectral lines estimates, and gives incorrect spectral estimation for time-series that are highly

Downloaded from http://gji.oxfordjournals.org/ at Vienna University Library on April 11, 2014

periodic (Lysne & Tjostheim 1987; de Hoon *et al.* 1996; Schlögl 2006).

The power spectra S_A is then obtained from the AR coefficients a^k and the variance of the AR model noise σ_y^2 by

$$S_A(f) = \frac{{\sigma_y}^2}{\left|1 - \sum_{k=1}^{p} a^k \mathrm{e}^{-i2\pi kf/f_s}\right|^2}, \quad (2)$$

where f is the dominant frequency, f_s is the sampling frequency, k is the order of the AR model controlling the frequency of the complex sinusoid and $i = \sqrt{-1}$.

Classical AR methods use the same number of time-invariant coefficients for the complete signal. Hence, it is assumed that the signal frequency content is stationary over the complete duration of the signal. We are here interested in looking at localized frequency content and rapid changes in resonance frequencies. Using the same idea as for the STFT, the AR method can be applied on shorter, overlapping segments of the signal, allowing the coefficients to change from one window to another. Using this technique we will be able to map quick changes in the frequency content, even though the signal frequency content is still assumed to be piecewise stationary inside each window.

AR methods rely mainly on the number of coefficients of the AR filter and on the position and length of the window of signal (w_l) on which the algorithm is applied (Ulrych & Bishop 1975). Too low a number of coefficients will smooth out the estimated spectra; conversely a high number of coefficients may introduce artificial peaks and spectral line splitting (Kay & Marple 1979, 1981). The order of the AR filter is then often estimated using information theory-based criteria, such as the final prediction error or Akaike Information Criteria (Priestley 1994). In practice however, these criteria have been found to regularly give erroneous estimations (Jones 1976; Berryman 1978) and the order selection eventually requires some experience from the user. It is commonly assumed that the AR order should not exceed $N/3$, where N is the number of samples of the time-series.

To optimize these two interdependent parameters (p, w_l), we minimize the squared difference between the normalized AR power spectral density (PSD) $\hat{S}_A$ and Fourier PSD $\hat{S}_F$. S_A is computed by eqs (1) and (2) using the Burg method for a realistic set of values of filter orders p, and window length w_l, within each time segment. The same window size and position are used to compute $\hat{S}_F$. We then search for the minimum of this 2-D cost function in a least-squares sense to determine the optimal values (Fig. 1). The minimum of the residuals calculated using the $L2$-norm can be expressed as

$$r(p, w_l) = \underset{p,w_l}{\operatorname{argmin}} ||\hat{S}_F(w_l) - \hat{S}_A(p, w_l)||_2, \quad (3)$$

where we dropped the dependence of $\hat{S}_A$ and $\hat{S}_F$ on frequency to simplify the notations.

The application of eq. (3) leads to the selection of high AR orders when the noise level is high. This is typically the case for the Fourier spectra of short time-series which are strongly contaminated by side-lobe leakage. For stationary spectral lines, a simple way to increase the signal contribution to the frequency spectrum while decreasing the one of random noises is to increase the window length, but more data are not always available. On the other hand, we can use *a priori* information to guide the selection of the optimal parameters. In particular, the AR order should be high for broad-band spectra and low for narrow-band spectra. We modify eq. (3) by including a criterion to account for the spectral bandwidth: $N_{\mathrm{bw}} = \frac{N_v \times \Delta f}{F_{\mathrm{Ny}}}$. This criterion corresponds to the width of the computed spectra,

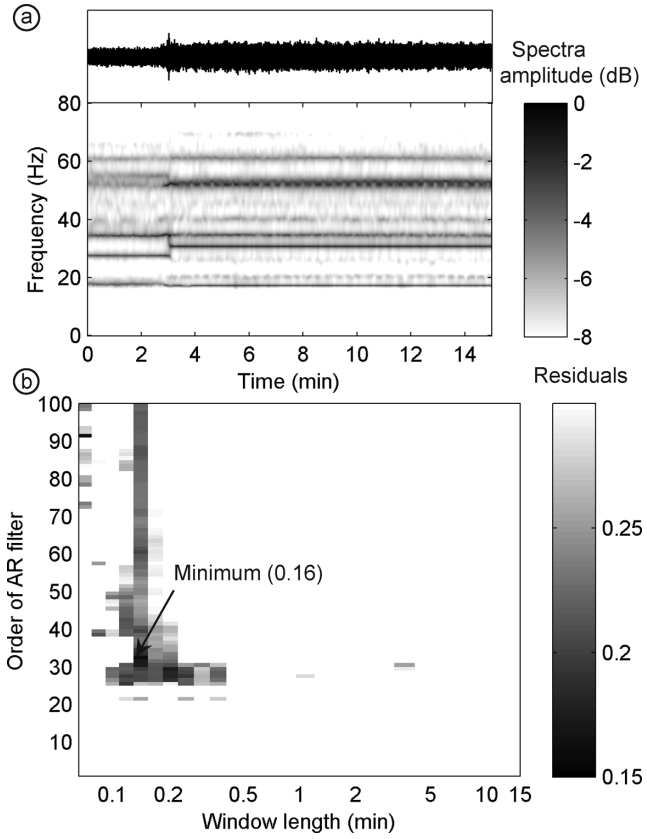

Figure 1. Example of optimal parameters selection for 15 min of signals from a microseismic experiment. (a) Raw data and time–frequency representation obtained using the ST-AR method with an overlap of 90 per cent and the optimal parameters given in (b). (b) 2-D cost function. The minimum of the 2-D cost function is indicated. The optimal order of the AR filter is 32 and the optimal window length is ∼8 s.

which is the number of values N_v above a certain frequency times the frequency bin Δf (sampling frequency divided by the number of points of the Fourier spectra), divided by the Nyquist frequency F_{Ny}. Here, N_v corresponds to all values of the spectrum above the full-width half-maximum (FWHM), that is, at –6 dB of the log-spectrum. The criterion N_{bw} is then incorporated into a Gaussian function, acting as a damping factor depending on the AR order p. Eq. (3) is then modified as

$$r(p, w_l) = \underset{p,w_l}{\operatorname{argmin}} \left\| \left[\hat{S}_F(w_l) - \hat{S}_A(p, w_l) \right] \times D \right\|_2,$$

$$\text{with } D = 1.1 - \mathrm{e}^{-\frac{[p-(N_{\mathrm{bw}} \times p_{\max})]^2}{2\times(0.5p_{\max})^2}}, \quad (4)$$

and where $p_{\max}$ is the maximum value of the AR order p. The number 1.1 prevents the Gaussian function to reduce the residuals too strongly for a range of p. This value ensures the weighting to vary between 0.1 and 1.1. The factor $N_{\mathrm{bw}} \times p_{\max}$ controls the position of the average of the Gaussian on the p-axis, while $0.5p_{\max}$ controls its width.

Finally, the AR coefficients for the model order p and window length w_l that minimizes eq. (4) provide the desired time–frequency representation $S_A(f, t)$ by assigning each individual spectrum to the time of each segment (Fig. 2). In the next section, we describe another AR method based on a recursive scheme for the Kalman filter. This method has the advantage to define AR coefficients at all data samples, increasing significantly the time resolution.

Downloaded from http://gji.oxfordjournals.org/ at Vienna University Library on Apr

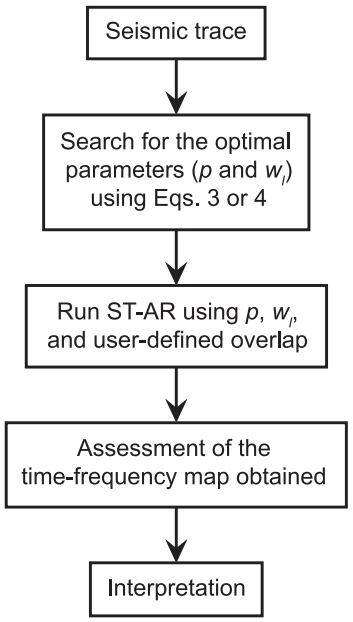

Figure 2. Flow chart step-by-step of the ST-AR algorithm. The order of the AR filter is indicated by p and the window length by w_l.

2.2 Kalman smoother

2.2.1 Description of the state-space model

In the following equations, scalars are represented by small letters, matrices by capital letters, vectors by bold letters, transpose matrices or vectors by an apostrophe, and estimates by a hat. In order to improve the time resolution of the ST-AR, an alternative is to treat the autoregressive coefficients as time dependent variables. Eq. (1) then becomes

$$y_n = \sum_{k=1}^{p} a_n^k y_{n-k} + v_n, \tag{5}$$

where a_n^k are the time-varying coefficients of the AR filter.

Two main approaches exist to introduce time-varying coefficients in the classical AR methods, namely the stochastic and deterministic regression approaches (Kaipio & Karjalainen 1997). The deterministic regression approach consists of introducing a linear combination of time-varying basis functions, such as power functions, Fourier series (e.g. Hall *et al.* 1983; Eom 1999) and prolate spheroidal sequences (Grenier 1983; Härmä *et al.* 2000), instead of time-invariant coefficients. The stochastic approach uses recursive algorithms, such as the recursive least squares or the Kalman filter, to estimate the AR coefficients at all times (e.g. Isaksson *et al.* 1981; Baziw & Weir-Jones 2002; Naghizadeh & Sacchi 2009). These methods are well known in the biomedical field (Bohlin 1977; Oikonomou *et al.* 2007), and for mechanical systems diagnosis for example (Conforto & D'Alessio 1999). However, typical AR orders in their cases are below 10 whereas in seismology, the AR orders often exceed 15–20 (Leonard & Kennett 1999). Here, eq. (5) is transformed into a state-space model in order to use the Kalman filter optimization equations:

$$\begin{aligned} &\text{Measurement equation}: y_n = \boldsymbol{m}_n' \boldsymbol{x}_n + \varepsilon_n, \\ &\text{Transition equation}: \boldsymbol{x}_n = T\boldsymbol{x}_{n-1} + \boldsymbol{\eta}_n, \end{aligned} \tag{6}$$

where $\boldsymbol{m}_n$ is a vector containing the previous p measurements, $\boldsymbol{x}_n$ is the state vector containing the AR coefficients and is assumed to be a Gauss–Markov process, ε_n and $\boldsymbol{\eta}_n$ are the independent and identically distributed AR and state noise, respectively. The AR and state noise are normally distributed, random variables with zero mean and variance σ_y^2 and Q, respectively. T is the transition matrix linking the previous state estimate to the following one.

Finally, the number of coefficients of the AR filter p is determined in the same way as the ST-AR method. The initial state $\boldsymbol{x}_0$ of the model is assumed to be Gaussian with mean $\boldsymbol{\mu}_0$ and covariance P_0, and independent of both the state and AR noises. In order to avoid any confusion, the state-space model parameters $\Theta \equiv \left\{T, \sigma_y^2, Q, \boldsymbol{\mu}_0, P_0\right\}$ and the coefficients of the AR model will be referred to as 'parameters' and 'coefficients', respectively.

2.2.2 Algorithm description

The KS algorithm is adapted from the expectation maximization KS (EMKS) algorithm described in detail in Ghahramani & Hinton (1996) and Khan & Dutt (2007). The complex expectation maximization scheme was found to bring little improvements to the AR model estimation and was therefore disregarded, keeping only the KS algorithm. Hereafter, we give the key relationships and indicate how the algorithm is adapted to seismological data.

The Kalman filter is a recursive process constituted by two sets of equations, the prediction and updating equations (Grewal & Andrews 2001). The conditional expectations of the state $\hat{\boldsymbol{x}}_{n|k}$ and associated error covariance $P_{n|k}$ given the data sequence $\boldsymbol{y}_{1:k} = [y_1, \ldots, y_k]$ are defined by

$$\begin{aligned} \hat{\boldsymbol{x}}_{n|k} &= E\left(\boldsymbol{x}_n | \boldsymbol{y}_{1:k}\right), \\ P_{n|k} &= E\left[\left(\boldsymbol{x}_n - \hat{\boldsymbol{x}}_{n|k}\right)\left(\boldsymbol{x}_n - \hat{\boldsymbol{x}}_{n|k}\right)' | \boldsymbol{y}_{1:k}\right], \end{aligned} \tag{7}$$

where E is the expectation operator. These notations, for example, $\hat{\boldsymbol{x}}_{n|n-1} = E\left(\boldsymbol{x}_n | \boldsymbol{y}_{1:n-1}\right)$ is the conditional expectation of $\boldsymbol{x}_n$ given the time-series $\boldsymbol{y}_{1:n-1} = [y_1, ..., y_{n-1}]$, are used in all the following equations. Given the state $\hat{\boldsymbol{x}}_{n-1|n-1}$ and associated error covariance $P_{n-1|n-1}$ estimates for the previous sample, the optimal state and error covariance estimates $\left[\hat{\boldsymbol{x}}_{n|n-1}, P_{n|n-1}\right]$ for the next time sample n are obtained via the Kalman filter prediction equations:

$$\begin{aligned} \hat{\boldsymbol{x}}_{n|n-1} &= T\hat{\boldsymbol{x}}_{n-1|n-1}, \\ P_{n|n-1} &= T P_{n-1|n-1} T' + Q. \end{aligned} \tag{8}$$

These estimates are then updated using the sample at instant n, incorporated in $\boldsymbol{m}_n$, via the Kalman filter updating equations:

$$\begin{aligned} K_n &= P_{n|n-1}\boldsymbol{m}_n' \left(\boldsymbol{m}_n P_{n|n-1} \boldsymbol{m}_n' + \sigma_y^2\right)^{-1}, \\ \hat{\boldsymbol{x}}_{n|n} &= \hat{\boldsymbol{x}}_{n|n-1} + K_n\left(y_n - \boldsymbol{m}_n \hat{\boldsymbol{x}}_{n|n-1}\right), \\ P_{n|n} &= \left(I - K_n \boldsymbol{m}_n\right) P_{n|n-1}, \end{aligned} \tag{9}$$

where K_n is the optimal Kalman gain. The updated state and error covariance estimates $\left[\hat{\boldsymbol{x}}_{n|n}, P_{n|n}\right]$ are then used in eq. (8) as $\left[\hat{\boldsymbol{x}}_{n-1|n-1}, P_{n-1|n-1}\right]$ for the next recursion. The forward recursions using the complete time-series and eqs 8 and 9 correspond to the Kalman filter scheme. The transition matrix (T), and the state (Q) and AR (σ_y^2) noise covariances are not updated at each recursion of the Kalman filter. For the first recursion, $\hat{\boldsymbol{x}}_{1|0} = \boldsymbol{\mu}_0$ and $P_{1|0} = P_0$.

The Kalman filter estimates can be further refined using the Rauch–Tung–Striebel backward recursions to obtain smoothed estimates (Rauch *et al.* 1965). The backward pass proceeds from the last sample N to the first sample and use the estimates saved during

Downloaded from http://gji.oxfordjournals.org/ at Vienna University Library on April 11, 2014

the forward pass. The backward recursions are given by

$$\begin{aligned} J_n &= P_{n|n} T' P_{n+1|n}^{-1}, \\ \hat{\boldsymbol{x}}_{n|N} &= \hat{\boldsymbol{x}}_{n|n} + J_n \left(\hat{\boldsymbol{x}}_{n+1|N} - \hat{\boldsymbol{x}}_{n+1|n} \right), \\ P_{n|N} &= P_{n|n} + J_n \left(P_{n+1|N} - P_{n+1|n} \right) J_n', \end{aligned} \tag{10}$$

where the index $n + 1$ refers to the estimates for the previous sample, n refers to the current sample, and N refers to the estimates updated through the backward pass. In eq. (10), $\left[\hat{\boldsymbol{x}}_{n+1|n}, P_{n+1|n}\right]$ correspond to the prediction estimates $\left[\hat{\boldsymbol{x}}_{n|n-1}, P_{n|n-1}\right]$ in eq. (8), after rearranging the indices for the backward pass, and $\left[\hat{\boldsymbol{x}}_{n|n}, P_{n|n}\right]$ are the updated estimates. The updated estimates for the last sample at $n = N$ are used as initial smoothed estimates $\left[\hat{\boldsymbol{x}}_{N|N}, P_{N|N}\right]$. The forward and backward recursions together constitute the Kalman smoother.

In practice, the model parameters need to be initialized before using the KS recursions. The transition matrix T is set to the identity matrix, while the other model parameters of Θ are evaluated using eq. (1) and the Burg method on a training data set. As there is only a single realization in the case of microseismic or volcano monitoring, and because we are interested in phenomena such as resonance frequencies that have long durations, we divide the time-series in segments ($\sim$10) of equal length and used them as our training data set. The initial value for each parameter is then the mean of the values obtained. These parameters can be used directly as inputs for the first recursion of the KS to obtain the optimal estimates of the AR coefficients (option 1, KS_1). On the other hand, all the initial parameters of Θ can be first refined using the KS on the training data set, and then used as inputs for the KS applied on the complete time-series (option 2, KS_2, Fig. 3).

Finally, the AR coefficients at all samples n together with the estimate of the variance of the AR model noise $\hat{\sigma}_y^2$ can be used to compute the time–frequency map in a similar way to eq. (2) using

$$S_{KS}(n, f) = \frac{\hat{\sigma}_y^2}{\left| 1 - \sum_{l=1}^{p} \hat{a}_n^k \mathrm{e}^{-i2\pi kf/f_s} \right|^2}. \tag{11}$$

No segmentation is involved in this method, allowing the determination of the frequency content of the time-series for each sample. However, the time resolution will not be equal to the sample rate due to the refinement of the KS estimates using the complete time-series, avoiding sudden jumps in the values of the AR coefficients.

The signal can then be reconstructed directly from the time-series using eq. (5) or by using the fact that the AR coefficients correspond also to the coefficients of an all-pole filter (e.g. Makhoul 1975; Kay & Marple 1981). To estimate quantitatively the reconstruction errors, we use the mean square error MSE given by

$$\mathrm{MSE} = \frac{1}{N} \sum_{n=1}^{N} |\hat{y}_n - y_n|^2, \tag{12}$$

where N is the number of samples, y_n is the original signal and $\hat{y}_n$ is the estimated signal.

In the next section, we will apply the two methods based on AR models as well as the STFT to a synthetic example, a volcano signal and a continuous recording from a microseismic experiment to assess their performances.

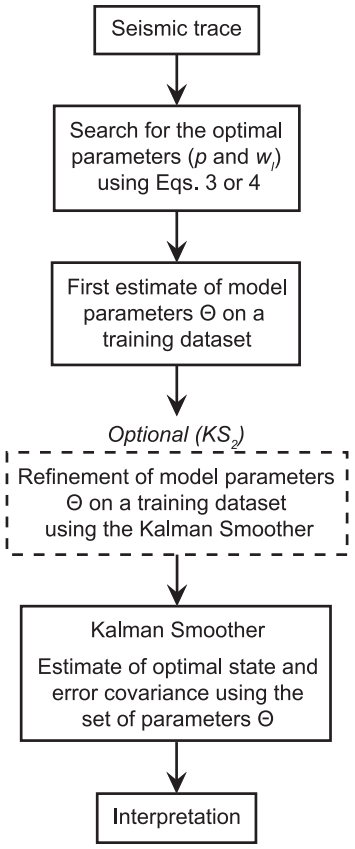

Figure 3. Flow chart step-by-step of the KS algorithm. The model parameters are indicated by Θ.

3 APPLICATIONS

3.1 Synthetic signal

To show the performance of each method, we created a synthetic signal with one harmonic at 5 Hz between 0 and 6 s, one harmonic at 15 Hz from 0 to 2 s that linearly changes from 15 to 20 Hz between 2 and 4 s, and stays at 20 Hz between 4 and 6.35 s, and two frequency modulated harmonics around 10 and 33 Hz between 6 and 10.2 s and between 2 and 6.4 s, respectively (Fig. 4). The harmonics amplitudes are as follows: 0.5 (5 Hz), 0.8 (15 and 20 Hz), 1 (chirp between 15 and 20 Hz), 0.7 (10 Hz) and 0.4 (33 Hz). This synthetic signal is then corrupted by random noise of variance 0.1 (maximum and minimum amplitudes of ± 1.5). Depending on the part of signal under consideration, the SNR, as defined by the ratio of the signal-to-noise amplitudes, is then between 1 and 4. This is a representative and challenging synthetic signal since it contains multiple constant and non-stationary resonance frequencies as well as high amplitude noise.

We determine the AR order using eqs (3) and (4) for orders between 1 and 100 and window lengths between 0.2 and 10.2 s. Using eq. (3), the optimal order is 35 whereas using eq. (4), the optimal order is 10. An AR order of 35 is obviously too high to estimate the frequency components of the synthetic signal presented in Fig. 4. This high AR order is due to the AR model trying to match the distortions introduced by the Fourier transform of the windowed signal as well as the random noise.

The AR order estimated using eq. (4) is more realistic and used to compute the time–frequency representation of the synthetic signal

Downloaded from http://gji.oxfordjournals.org/ at Vienna University Library on Apr

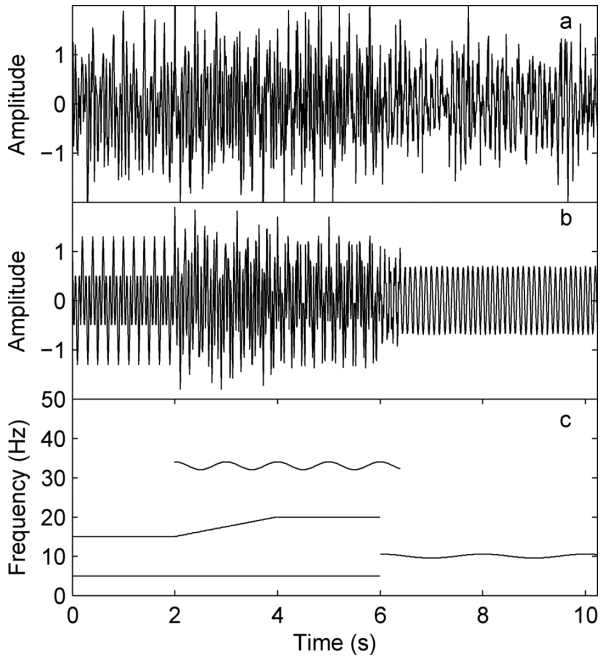

Figure 4. (a) Synthetic signal corrupted by random noise (variance: 0.1), (b) noiseless synthetic signal and (c) instantaneous frequencies of the noiseless signal.

using the ST-AR and KS methods. A comparison of the different time–frequency maps is given in Fig. 5. Hereafter, we used a window length for the STFT that corresponds to our best compromise between the reduction in spectral smearing (frequency resolution), time resolution and the readability of the different frequency components.

The STFT is able to retrieve the constant harmonics at 5 and 15 Hz, the linear change from 15 to 20 Hz, as well as the frequency modulated harmonic around 10 Hz with reasonable accuracy. Even the oscillations around the spectral line at 33 Hz are discernible. Compared with the STFT, the ST-AR is able to map the low frequency lines with somewhat less smearing, even though the frequency modulated component at 33 Hz is not as well recovered. The background noise of the ST-AR representation is significantly lower than the one of the STFT.

The initial model parameters for the KS are determined using a training data set consisting in 100 realizations of the synthetic signal with high-amplitude random noise (noise variance of 0.2). These parameters are then introduced into the KS scheme. All frequency components are detected by the KS_2, including the linear change from 15 to 20 Hz, but the time–frequency map is smoother than those of the other methods and the frequency modulations are lost. The KS_1 gives a more accurate picture. However, without the smoothing introduced by the refinement of the AR coefficients estimate on the training data set by the KS, the KS_1 representation exhibits high-frequency oscillations in frequency and discontinuous frequency estimates, which are due to the random noise.

The signals reconstructed from the AR coefficients are presented in Fig. 6. In the case of the KS method, the signal was reconstructed for every sample using the backward prediction of eq. (5). For the ST-AR method, the AR coefficients are given for a segment of signal allowing to use the filter approach to reconstruct the estimated signal (Makhoul 1975; Kay & Marple 1981).

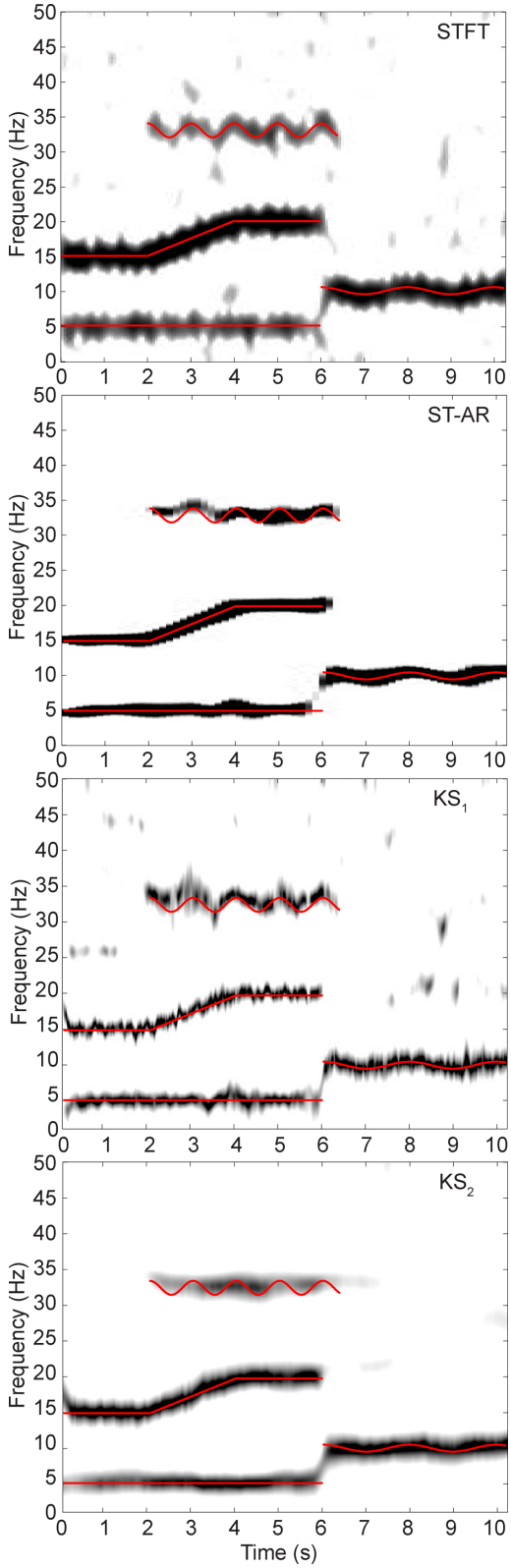

Figure 5. Time–frequency representations of the synthetic signal given in Fig. 4, obtained using the STFT with a window of 0.6 s and an overlap of 90 per cent, the ST-AR with an AR order of 10, a window of 1.6 s and an overlap of 90 per cent, and the KS_1 and KS_2 methods with an AR order of 10. The instantaneous frequencies of the noiseless synthetic signals are superimposed to the time–frequency representations (red lines).

Downloaded from http://gji.oxfordjournals.org/ at Vienna University Library on April 11, 2014

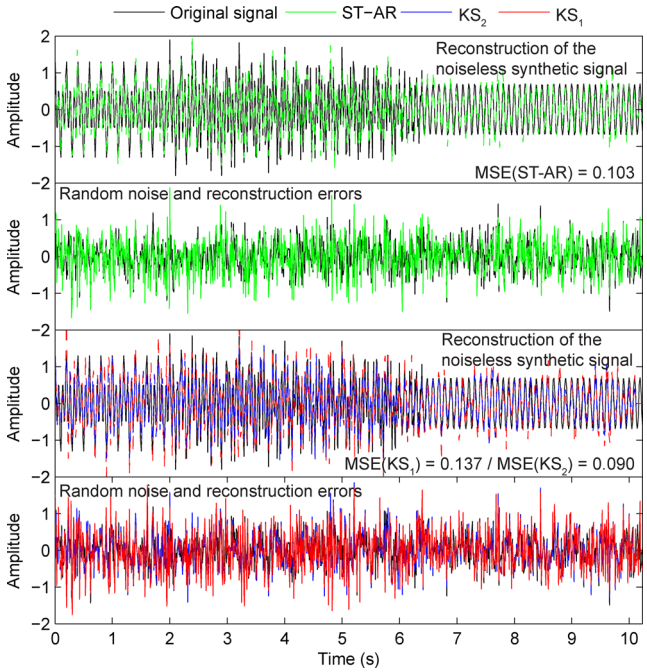

Figure 6. Reconstruction of the synthetic signal from the AR coefficients used for the time–frequency representations of Fig. 5. Top row: reconstruction of synthetic seismogram for the ST-AR method (green) and true noiseless signal (black). Second row: added random noise (black) and reconstruction error (green) for ST-AR results. Third row: reconstruction of synthetic seismogram for KS_1 (red) and KS_2 (blue) methods and true noiseless signal (black). Last row: added random noise (black) and reconstruction errors for KS_1 (red) and KS_2 (blue) results.

The amplitude of the signal reconstruction residuals, including the reconstruction errors and the random noise, is of the order of the amplitude of the introduced random noise (Fig. 6). For reference, the MSE (eq. 12) obtained by only bandpassing the data between 2 and 40 Hz is approximately 0.16. The method with the smallest MSE is the KS_2 method (∼0.09), followed by the ST-AR (∼0.103) and KS_1 (∼0.137) methods. It roughly corresponds to 4–7 per cent of the maximum amplitude of the signal. Regarding the frequency variations, the three methods are able to reconstruct all signal components (Fig. 6). The STFT and the various AR methods have then different objectives. The STFT would represent the noisy signal in Fig. 4(a), while AR methods attempt to retrieve the noiseless signal shown in Fig. 4(b).

3.2 Long-period volcanic event

In order to show the applicability and the performance of these methods to other seismic signals, we choose to apply them on LP volcanic events for their well-known spectral characteristics and overall importance in volcano hazard management. LP volcanic events generally start with a high-frequency component, with a broader spectra, followed by a tail constituted by few harmonics in a frequency range between 0.5 and 10 Hz (Chouet 1996). Unlike volcano-tectonic events, which correspond to brittle or tensile failure in the solid part of the volcano, LP events are related to the resonant behaviour of fluid-filled cavities or conduits triggered by pressure variations (Chouet 1996; Benson *et al.* 2008). LP events and tremors recorded at volcanoes typically share the same spectral signature even if they have different durations, possibly indicating a common source mechanism.

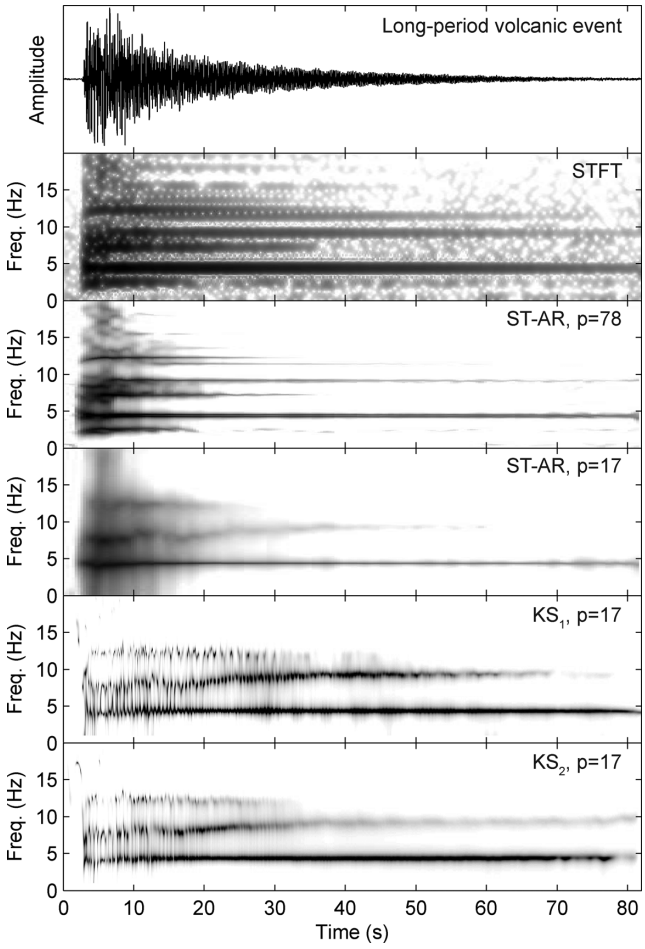

Figure 7. LP volcanic event recorded at Misti volcano, Peru (Lesage *et al.* 2002). From top to bottom are given the raw data, the time–frequency representations of this signal obtained using the STFT (window: 1 s, overlap: 90 per cent), the ST-AR (AR orders: 78 and 17, window: 2 s, overlap: 90 per cent), the KS_1 and KS_2 methods (AR order: 17). The two AR orders obtained using eqs (3) and (4) are 78 and 17, respectively.

The LP volcanic event presented in this section was recorded at Misti volcano, Peru (Fig. 7). The spectral content of this event has been analysed by Lesage *et al.* (2002) with different techniques such as the STFT, the CWT and AR models. This event is about 80 s long and constituted by an onset (2.5–10 s) with a broader spectra and five main harmonics at 2.6, 4.5, 7.3, 9.5 and 12.4 Hz; the spectral line at 4.5 Hz having the highest amplitude. The different spectral lines are mostly linear on all time–frequency decompositions. Some of them are shifting (12.5–11.5 Hz) or are discontinuous (2.6 Hz).

The STFT representation, computed using a window of 1 s with an overlap of 90 per cent, displays the main features of the event (broad onset and harmonics). The AR order obtained using eq. (3) and eq. (4) are 78 and 17, respectively. The AR order obtained using eq. (4) is consistent with the AR order found by Lesage (2008) (18) for the same event, using the kurtosis of the deconvolved signal. We used an AR order of 17 to compare the decomposition results of KS_1 and KS_2 methods with the other methods.

Compared with the ST-AR representation with 78 AR coefficients, the STFT representation is noisier and shows some smearing around the main frequency lines. The other AR methods computed with 17 AR coefficients are able to map accurately two of the harmonics (4.5 and 12.4 Hz). The spectral line in between shifts progressively from 7.4 to 9.4 Hz, showing that these two lines are

Downloaded from http://gji.oxfordjournals.org/ at Vienna University Library on Apr

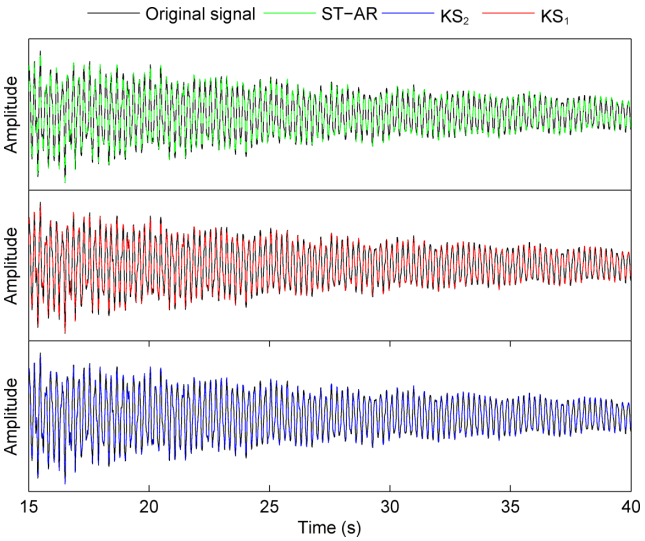

Figure 8. Reconstruction of a part of the long-period volcanic event with well-defined harmonics, from 15 to 40 s, from the estimated AR coefficients used for the time–frequency maps shown in Fig. 7 with an AR order of 17.

too close to be represented by 17 AR coefficients only. The KS_2 representation also appears smoother than the one of KS_1 due to the additional refinement of the AR coefficients on the complete time-series (Fig. 7).

The reconstruction of a part of the LP event with well-expressed harmonics is shown in Fig. 8. Even with only 17 AR coefficients, the reconstructed signals are very close to the original one. The time–frequency decompositions using 17 AR coefficients represent a large amount of the LP event energy, even if they show a different behaviour from the STFT. The various outcomes demonstrate the value of applying different time–frequency transforms to the same signal to validate its characteristics.

3.3 Microseismic data set

In this section, the three methods, STFT, ST-AR and KS_2, are applied to a microseismic data set having a high-amplitude noise (Fig. 9). The results of the KS_1 method will not be shown here because this method is efficient for signals with a high SNR, and gave very blurry images of these data samples.

The present data set is a two-stage experiment recorded by 12 three-components regular geophones at a sampling frequency of 4000 Hz. The geophones were deployed in a vertical well at a depth similar to the one of the fluid injection. As no theoretical evaluation of each method is available, we will compare these methods using typical problems encountered in microseismic experiments analysis.

(i) Time and frequency resolutions.
(ii) Noise sensitivity.
(iii) Ability to track time-varying frequency contents.

Five minutes of the second stage of this microseismic experiment, showing step-like and smooth variations in spectral lines, was selected to compare the outcomes of each method using the STFT as a reference. A window length of 4 s with 90 per cent overlap was used to compute the STFT. The associated time resolution is of the same order. The time–frequency representation shows four main resonance frequencies at ∼18, ∼31, ∼35 and ∼52 Hz. Lower amplitude lines are present at ∼60 Hz and between the lines at ∼31 and ∼35 Hz. Apart for the lines at ∼60 and ∼35 Hz, all the other

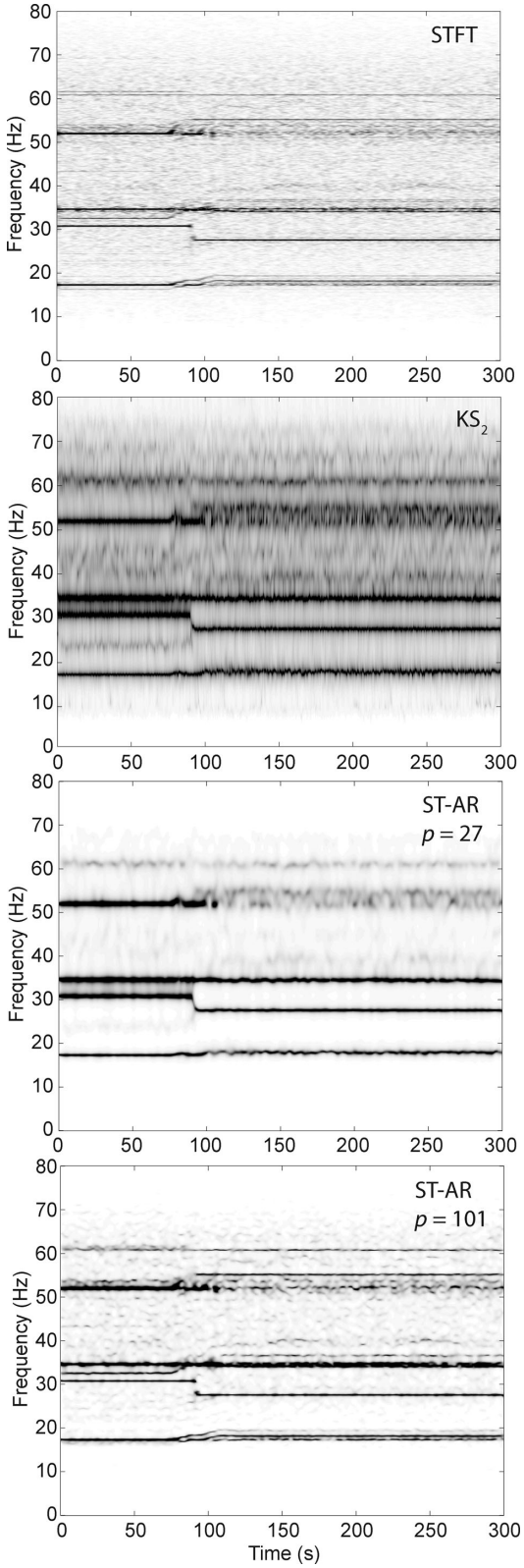

Figure 9. STFT, ST-AR and KS_2 methods applied to a microseismic data segment of 5 min (vertical component of the deepest geophone). The data are downsampled from 4000 to 160 Hz prior to the computation. Black parts correspond to high amplitudes. STFT and ST-AR methods are computed using a window of 4 s and an overlap of 90 per cent. For the ST-AR, the two AR model orders used comes from eq. (3) ($p = 101$) and eq. (4) ($p = 27$). The KS_2 is computed using an AR model order of 27.

Downloaded from http://gji.oxfordjournals.org/ at Vienna University Library on April 11, 2014

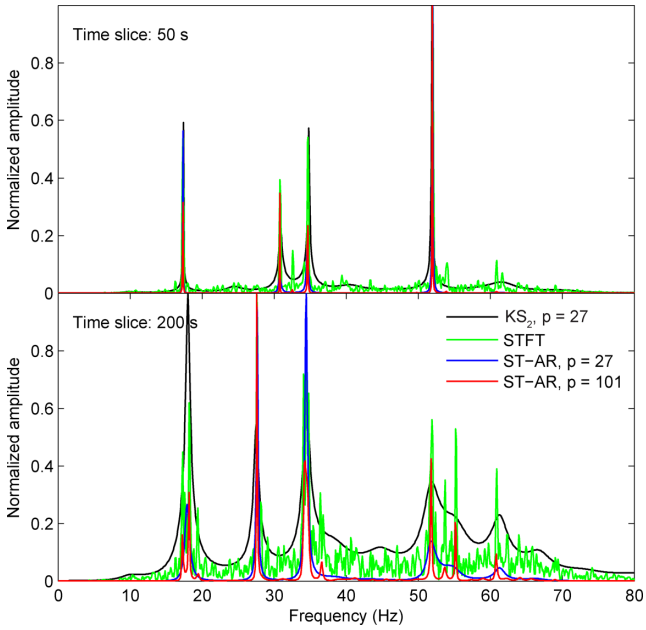

Figure 10. Normalized amplitude spectra for the three methods and two time slices at 50 and 200 s from Fig. 9. The STFT corresponds to the green line, the ST-AR to the blue ($p = 27$) and red ($p = 101$) lines, and the KS_2 to the black line.

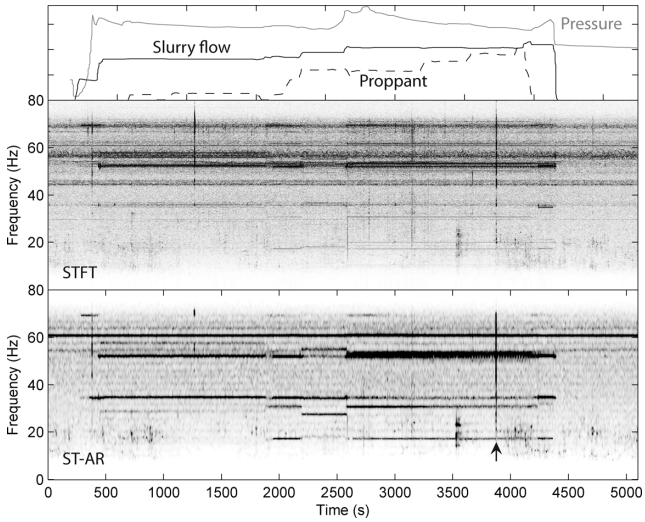

Figure 11. Treatment conditions as well as time–frequency representations of a complete microseismic data set (horizontal component of the fifth geophone) using STFT and ST-AR methods. Both methods are computed using a window of 10 s with an overlap of 90 per cent. The ST-AR is computed with an AR order of 54 (eq. 3). The vertical arrow indicates a signal with a sharp onset corresponding to a *P*-wave travelling downward in the casing of the observation well.

spectral lines change at ∼95 s. This change is correlated with an increase in the slurry injection rate. We observe different changes depending on the spectral line. The spectral line at ∼52 Hz almost disappears or shifts to ∼54 Hz, the one at ∼31 Hz drops suddenly to ∼27 Hz, and the one at ∼18 Hz increases smoothly while splitting in a few lines. The background noise, coming from both the data and spectral leakage, manifests itself by the blurry aspect of the time–frequency plot (Fig. 10).

The ST-AR is computed using a window length of 4 s with 90 per cent overlap (Fig. 9). The optimum number of coefficients is 101 using eq. (3) and 27 using eq. (4). The four main resonance frequencies are clearly visible on Fig. 9 with both AR model orders. They follow the same pattern as the one shown by the STFT. However, regarding the lines of smaller amplitudes, even though the line at ∼60 Hz is present, the one between the lines at ∼31 and ∼35 Hz is absent for the AR order of 27. This arises from the design of the method itself which uses a polynomial of order p to fit the data, at the expense of the obliteration of very close frequency lines. When the ST-AR is applied with an AR order of 101, the spectral resolution of the ST-AR is similar to the one of the STFT and all spectral lines are present. In both cases, the background noise is generally lower than the one of the STFT (Figs 9 and 10). The identification of resonances is then facilitated compared to the STFT.

The KS_2 is computed using an AR order of 27 (Fig. 9) because the computation of the KS_2 with an AR order of 101 is computationally expensive. Similarly to the ST-AR with an AR order of 27, the four main resonance frequencies as well as the line at ∼60 Hz are present but not the frequency line between the lines at ∼31 and ∼35 Hz. The background noise is higher for the KS_2 compared to the ST-AR and the STFT, this method showing a spectrum following the one of the STFT (Fig. 10). A spectral line that is not identifiable on the STFT and ST-AR figures, is visible at ∼24 Hz between 0 and 95 s and may be an artifact. The evolution of the AR coefficients is computed for all samples, leading to a better time resolution than the other methods. In return, due to the recursive nature of the algorithm and the size of the arrays involved, the computational cost of this algorithm is higher than those of the STFT and ST-AR.

In order to test the performance of the STFT and the ST-AR on a long time-series with low-amplitude spectral lines, we apply the two methods to the complete microseismic experiment of ∼1.5 hr recorded by the horizontal component of another geophone (Fig. 11). The same window length (10 s) and overlap (90 per cent) are used for the two methods. The AR order determined using eq. (3) is 54. The time–frequency picture given by the STFT is contaminated by high-amplitude noise above 40 Hz, while low-amplitude spectral lines are visible around ∼18, ∼31 and ∼35 Hz. The resonances above 40 Hz are hardly identifiable due to the noise. On the other hand, the low noise level of the ST-AR representation facilitates the identification of the different resonances. Signals with sharp onsets, corresponding to vertical lines on time–frequency maps, are also displayed by the ST-AR (Fig. 11).

4 DISCUSSION

The results of AR methods depends on the procedure to determine their optimal parameters (Figs 2 and 3). In the case of the AR order selection using eqs (3) and (4), a comprehensive sampling of the possible pairs p and w_l is necessary to obtain a good estimate of the optimal parameters. We tested all AR orders from 1 to 100 or 1 to 150 and around 30 windows lengths depending on the length of the time-series under consideration. For short signals, we recommend the damped estimate obtained using eq. (4) to prevent biases due to spectral leakage in the FFT to dominate the inversion results. One can also use a low AR order for large amount of data when a low-resolution time–frequency picture is desired, or for time-consuming algorithms such as the KS. When computing the ST-AR, the window length is less important than the AR order. A rule of thumb is that the length of the analysis window can be set to four to six times the AR order p.

For longer time-series, we recommend eq. (3) to estimate the number of AR poles. This equation leads to a larger number of

Downloaded from http://gji.oxfordjournals.org/ at Vienna University Library on Apr

estimated AR poles but noise sensitivity or spectral line splitting are minor items due to the large number of samples (e.g. Figs 9 and 11). A larger number of poles can also provide more detailed pictures and handle more easily the appearance of new resonances. Overall, even if computationally more consuming than Akaike's criteria, AR order selection using eqs (3) and (4) was found to give reasonable results.

Most of the frequency components for both short and long signals are recovered by the STFT, the ST-AR and the KS_2. Smooth and sharp variations in frequency are correctly represented as well. Even though spurious peaks and spectral line splitting are common for AR spectral estimates (Kay & Marple 1981), the consistency between AR and Fourier spectral estimations shows that the LP event harmonics and the resonances in our microseismic data can be described by an AR model. Despite its shortcomings due to signal windowing (width of the main lobe and side-lobe leakage), the STFT gives reasonable results even in the presence of high amplitude noise. The KS_1 method gives reliable results only for time-series with a high SNR. The higher level of background noise of the KS_2 method is due to the smooth character of its spectral estimates (Fig. 10). In comparison to the other methods, the ST-AR shows the lowest level of background noise.

The main inconvenience of the KS_2 method is then the smearing of the spectral lines around their central frequency (Figs 5 and 7). The resulting loss in frequency resolution is not compensated by a better time resolution. Nevertheless, for the time–frequency representation of time-series of intermediate size, the KS_2 is able to detect the main resonance frequencies and reconstruct the signal with high fidelity. KS_2 and ST-AR methods fail to detect weak spectral lines when a low AR order is selected. The STFT results show a better spectral resolution in this case (Fig. 5) owing to the high flexibility of its algorithm. While the AR order can be increased for the ST-AR, this is not an option for the KS_2 due to its heavy computational scheme and the large memory requirements involved. Using high AR orders, the ST-AR is able to map both resonances and broadband signals (Fig. 11) even though the primary application of AR methods stays the modelling of spectral lines. Compared with both AR methods, the STFT provides robust spectral estimates using a simple and effective computational scheme.

The time resolution of the ST-AR method is the same as the STFT but its frequency resolution is not strictly inversely proportional to the window length or time resolution, even though the accuracy in frequency content estimation is still related to the length of the analysed window (e.g. Sakai 1979). Other techniques based on the Fourier transform, such as Welch's spectral averaging method (Welch 1967) or the multitaper method (Thomson 1982; Xiao & Flandrin 2007), can be used to decrease side-lobes spectral leakage even though they still show some spectral smearing. When long time-series are available, such as for the microseismic experiment, a long window can be employed and the spectral smearing in STFT representations is limited. The Wigner–Ville distribution is another method with a high time–frequency resolution. However, this method is also characterized by cross-terms without direct physical meaning. These terms can be attenuated at the expense of a decrease in time–frequency resolution (Cohen 1989). Some transforms, such as the CWT (Daubechies 1992) and the S-transform (Stockwell *et al.* 1996), have a variable time–frequency resolution depending on the frequency under investigation by keeping a constant ratio central frequency to frequency bandwidth. To reduce side-lobe leakage and improve localization, the S-transform uses a Gaussian taper while the CWT uses different wavelet families. These transforms are however still prone to spectral smearing, limited by the Gabor uncertainty principle (Hall 2006; Tary & van der Baan 2012).

The number of poles p is identical to half the number of resolved spectral peaks of the AR filter. For short time-series and low AR orders, the frequency resolution of the AR methods is therefore limited and comparable to that of the STFT. Other methods, like empirical mode decomposition (e.g. Flandrin *et al.* 2004; Han & van der Baan 2013) or the newly introduced synchrosqueezing transform (Daubechies *et al.* 2011) are preferable in this case. For long signals however, the increased frequency resolution combined with low noise sensitivity of the ST-AR allow an easy identification of the different time-varying frequencies (Fig. 11).

Applying different methods to the same time-series can help validate or invalidate the resulting time–frequency representations. While the STFT is commonly employed to obtain a first general picture of the frequency content, AR methods are designed to extract and reconstruct specific harmonics from time-series and can achieve a better time–frequency resolution in many circumstances. The damping of resonances, measured by their quality factor, can be estimated directly using the AR coefficients (Lesage *et al.* 2002). The quality factor Q is a frequency-domain measurement corresponding to the ratio central frequency to frequency bandwidth at –3 dB. High Q-factors characterize long-lasting harmonics with sharp spectral peaks. This factor have to be determined for a suitable range of AR order and for data windows with well-defined harmonics. It contains information on the source of the resonance, such as the geometry of the resonator and its fluid contents (Kumagai & Chouet 2000).

5 CONCLUSION

The two AR methods for spectral estimation presented here, namely the ST-AR and the KS, show consistent results although very different in details. Both methods are able to represent the time-varying frequency content of time-series, either by applying the Burg method for AR model estimation on short data segments, or by estimating recursively the AR coefficients for each new data sample with the Kalman smoother. The time–frequency map obtained depends mainly on the number of AR coefficients. Here, the AR order is selected based on the spectral comparison between the AR and Fourier spectra for a realistic set of parameters (AR order and signal window length and position). When a high level of noise is present, the AR order estimation can be damped with a Gaussian taper. The AR orders obtained using this simple procedure are suitable for describing and analysing the observed time-series.

The STFT is an effective and reliable method that can be applied to the time–frequency analysis of resonance frequencies, even in the presence of noise. The KS method gives accurate estimates of the main spectral components for time-series of short and intermediate size with an intermediate SNR, but its heavy computational scheme prevents its use for long time-series or with high AR orders. On the other hand, the ST-AR method combines high spectral resolution as well as low noise sensitivity with a flexible scheme. High AR orders can be used with this method for long time-series without introducing spectral line splitting or artificial peaks. AR coefficients also enable to reconstruct or remove some parts of the signal. Different parts of the signal are enhanced by the different methods allowing the identification of different frequency components (harmonics, localized wavelets...) or errors (spectral bias, spectral line splitting or spurious peaks).

Downloaded from http://gji.oxfordjournals.org/ at Vienna University Library on April 11, 2014

A better identification of resonance frequencies may help to gain a better understanding of the underlying physical mechanisms. An accurate estimation of the time-varying frequency content of microseismic experiments is of crucial importance because of the multiple causes of resonance frequencies during the fluid injection, each potential source being associated with a specific pattern. Resonance frequencies detection is usually further complicated by the high-amplitude noise present in microseismic recordings due to the pumping operations for example. Resonance frequencies, especially in the low-frequency band, may provide complementary information to the microseismic event distribution in order to better assess the deformation occurring during fracturing experiments, flow-back experiments, or CO_2 injection and storage. Likewise, a better time–frequency characterization of volcanic signals and in particular low-frequency tremors may help improve our understanding of their physical origin as well as aid in volcano hazard management.

ACKNOWLEDGEMENTS

The authors would like to thank the sponsors of the Microseismic Industry Consortium for financial support, and an anonymous company for permission to show and use their data. Constructive reviews by Hiroyuki Kumagai and two anonymous reviewers significantly improved the original manuscript.

REFERENCES

Aki, K., Fehler, M. & Das, S., 1977. Source mechanism of volcanic tremors: fluid-driven crack model and their application to the 1963 Kilauea eruption, *J. Volc. Geotherm. Res.,* **2**(3), 259–287.

Baziw, E. & Weir-Jones, I., 2002. Application of Kalman filtering techniques for microseismic event detection, *Pure appl. Geophys.,* **159,** 449–471.

Benson, P.M., Vinciguerra, S., Meredith, P.G. & Young, R.P., 2008. Laboratory simulation of volcano seismicity, *Science,* **322,** 249–252.

Berryman, J.G., 1978. Choice of operator length for maximum entropy spectral analysis, *Geophysics,* **43,** 1384–1391.

Bohlin, T., 1977. Analysis of EEG signals with changing spectra using a short-word Kalman estimator, *Math. Biosci.,* **35,** 221–259.

Bonnefoy-Claudet, S., Cotton, F. & Bard, P.-Y., 2006. The nature of noise wavefield and its applications for site effects studies: a literature review, *Earth-Sci. Rev.,* **79**(3–4), 205–227.

Burg, J.P., 1972. The relationship between maximum entropy spectra and maximum likelihood spectra, *Geophysics,* **37,** 375–376.

Chouet, B., 1986. Dynamics of a fluid-driven crack in three dimensions by the finite difference method, *J. geophys. Res., 91,* 13 967–13 992.

Chouet, B.A., 1996. Long-period volcano seismicity: its source and use in eruption forecasting, *Nature,* **380,** 309–316.

Claerbout, J.F., 1985. *Fundamentals of Geophysical Data Processing, with Applications to Petroleum Prospecting,* Blackwell, 266pp.

Cohen, L., 1989. Time-frequency distributions—a review, *Proc. IEEE,* **77**(7), 941–941.

Conforto, S. & D'Alessio, T., 1999. Spectral analysis for non-stationary signals from mechanical measurements: a parametric approach, *Mech. Syst. Signal Process.,* **13,** 395–411.

Das, I. & Zoback, M.D., 2011. Long-period, long-duration seismic events during hydraulic fracture stimulation of a shale gas reservoir, *Leading Edge,* **30,** 778–786.

Daubechies, I., 1992. *Ten Lectures on Wavelets,* CBMS-NSF Regional Conference Series in Applied Mathematics, Society for Industrial and Applied Mathematics.

Daubechies, I., Lu, J. & Wu, H.-T., 2011. Synchrosqueezed wavelet transforms: an empirical mode decomposition-like tool, *Appl. Comput. Harmonic Anal.,* **30,** 243–261.

Eom, K.B., 1999. Analysis of acoustic signatures from moving vehicles using time-varying autoregressive models, *Multidimensional Syst. Signal Process.,* **10,** 357–378.

Flandrin, P., Rilling, G. & Gonçalvés, P., 2004. Empirical mode decomposition as a filter bank, *IEEE Signal Process. Lett.,* **11,** 112–114.

Ghahramani, Z. & Hinton, G.E., 1996. *Parameter estimation for linear dynamical systems, Technical report,* University of Toronto, ON, Canada.

Grenier, Y., 1983. Time-dependent ARMA modeling of nonstationary signals, *IEEE Trans. acoust., Speech Signal Process.,* **31,** 899–911.

Grewal, M.S. & Andrews, A.P., 2001. *Kalman Filtering: Theory and Practice Using Matlab,* 2nd edn, Wiley-Interscience, 401pp.

Hall, M., 2006. Resolution and uncertainty in spectral decomposition, *First Break,* **24,** 43–47.

Hall, M.G., Oppenheim, A.V. & Willsky, A.S., 1983. Time-varying parametric modeling of speech, *Signal Process.,* **5,** 267–285.

Han, J. & van der Baan, M., 2013. Empirical mode decomposition for seismic time-frequency analysis, *Geophysics,* **78,** O9–O19.

Harris, F.J., 1978. On the use of windows for harmonic analysis with the discrete Fourier transform, *Proc. IEEE,* **66,** 51–83.

Härmä, A., Juntunen, M. & Kaipio, J.P., 2000. Time-varying autoregressive modeling of audio and speech signals, in *Proceedings of the EUSIPCO*, Tampere, Finland, pp. 2037–2040.

de Hoon, M.L.J., van der Hagen, T.H.J.J., Shoonewelle, H. & van Dam, H., 1996. Why Yule-Walker should not be used for autoregressive modelling, *Ann. Nucl. Energy,* **23,** 1219–1228.

Isaksson, A., Wennberg, A. & Zetterberg, L.H., 1981. Computer analysis of EEG signals with parametric models, *Proc. IEEE,* **69,** 451–461.

Jones, R.H., 1976. Autoregression order selection, *Geophysics,* **41,** 771–773.

Julian, B.R., 1994. Volcanic tremor: nonlinear excitation by fluid flow, *J. geophys. Res.,* **99**(B6), 11 859–11 877.

Kaipio, J.P. & Karjalainen, P.A., 1997. Estimation of event-related synchronization changes by a new TVAR method, *IEEE Trans. Biomed. Eng.,* **44,** 649–656.

Kay, S. & Marple, L., 1979. Sources and remedies for spectral line splitting in autoregressive spectrum analysis, *Proc, IEEE Int. Conf. Acoust. Speech Signal Process.,* **4,** 151–154.

Kay, S.M. & Marple, S.L. J., 1981. Spectrum analysis—a modern perspective, *Proc. IEEE,* **69,** 1380–1419.

Khan, M.E. & Dutt, D.N., 2007. An expectation-maximization algorithm based Kalman smoother approach for event-related desynchronization (ERD) estimation from EEG, *IEEE Trans. Biomed. Eng.,* **54,** 1191–1198.

Kumagai, H. & Chouet, B.A., 2000. Acoustic properties of a crack containing magmatic or hydrothermal fluids, *J. geophys. Res.,* **105**(B11), 25 493–25 512.

Lees, J.M., Gordeev, E.I. & Ripepe, M., 2004. Explosions and periodic tremor at Karymsky volcano, Kamchatka, Russia, *Geophys. J. Int.,* **158**(3), 1151–1167.

Lesage, P., 2008. Automatic estimation of optimal autoregressive filters for the analysis of volcanic seismic activity, *Nat. Hazards Earth Syst. Sci.,* **8,** 369–376.

Lesage, P., Glangeaud, F. & Mars, J., 2002. Applications of autoregressive models and time-frequency analysis to the study of volcanic tremor and long-period events, *J. Volc. Geotherm. Res.,* **114,** 391–417.

Leonard, M. & Kennett, B.L. N., 1999. Multi-component autoregressive techniques for the analysis of seismograms, *Phys. Earth planet. Inter.,* **113,** 247–263.

Lysne, D. & Tjostheim, D., 1987. Loss of spectral peaks in autoregressive spectral estimation, *Biometrika,* **74,** 200–206.

Makhoul, J., 1975. Linear prediction: a tutorial review, *Proc. IEEE,* **63,** 561–580.

Marple, S.L.J., 1982. Frequency resolution of Fourier and maximum entropy spectral estimates, *Geophysics,* **47**(9), 1303–1307.

Maxwell, S.C., Shemeta, J., Campbell, E. & Quirk, D., 2008. Microseismic deformation rate monitoring, in *Proceedings of the Annual Technical Conference and Exhibition, Society of Petroleum Engineers,* SPE 116596.

Muthuswamy, J. & Thakor, N.V., 1998. Spectral analysis methods for neurological signals, *J. Neurosci. Methods,* **83,** 1–14.

Naghizadeh, M. & Sacchi, M.D., 2009. F-X adaptive seismic-trace interpolation, *Geophysics,* **74,** V9–V16.

Downloaded from http://gji.oxfordjournals.org/ at Vienna University Library on Apr

Nakano, M., Kumagai, H., Kumazawa, M., Yamaoka, K. & Chouet, B.A., 1998. The excitation and characteristic frequency of the long-period volcanic event: an approach based on an inhomogeneous autoregressive model of a linear system, *J. geophys. Res.,* **103**(B5), 10 031–10 046.

Oikonomou, V.P., Tzallas, A.T. & Fotiadis, D.I., 2007. A Kalman filter based methodology for EEG spike enhancement, *Comp. Methods Prog. Biomed.,* **85,** 101–108.

Pettitt, W., Reyes-montes, J., Hemmings, B., Hughes, E. & Young, R.P., 2009. Using continuous microseismic records for hydrofracture diagnostics and mechanics, *SEG Expanded Abstract,* **28,** 1542–1546.

Priestley, M.B., 1994. *Spectral Analysis and Time Series,* Academic Press, 890pp.

Quirk, M. & Liu, B., 1983. *On the Resolution of Autoregressive Spectral Estimation,* IEEE ICASSP.

Rauch, H.E., Striebel, C.T. & Tung, F., 1965. Maximum likelihood estimates of linear dynamic systems, *AIAA J.,* **3,** 1445–1450.

Reine, C., van der Baan, M. & Clark, R., 2009. The robustness of seismic attenuation measurements using fixed- and variable-window time-frequency transforms, *Geophysics,* **74,** WA123–WA135.

Sakai, H., 1979. Statistical properties of AR spectral analysis, *IEEE Trans. Acoust., Speech, Signal Process.,* **27,** 402–409.

Schlögl, A., 2006. A comparison of multivariate autoregressive estimators, *Signal Process.,* **86,** 2426–2429.

Stockwell, R.G., Mansinha, L. & Lowe, R.P., 1996. Localization of the complex spectrum: the S Transform, *IEEE Trans. Signal Process.,* **44,** 998–1001.

Tary, J.B. & van der Baan, M., 2012. Potential use of resonance frequencies in microseismic interpretation, *Leading Edge,* **31,** 1338–1346.

Thomson, D.J., 1982. Spectrum estimation and harmonic analysis, *Proc. IEEE,* **70**(9), 1055–1096.

Ulrych, T.J. & Bishop, T.N., 1975. Maximum entropy spectral analysis and autoregressive decomposition, *Rev. Geophys. Space Phys.,* **13,** 183–200.

de Waele, S. & Broersen, P.M. T., 2000. The Burg algorithm for segments, *IEEE Trans. Signal Process.,* **48,** 2876–2880.

Welch, P.D., 1967. The use of fast Fourier transform for the estimation of power spectra: a method based on time averaging over short, modified periodograms, *IEEE Trans. Audio Electroacoust.,* **AU-15,** 70–73.

West, M.E., Larsen, C.F., Truffer, M., O'Neel, S. & LeBlanc, L., 2010. Glacier microseismicity, *Geology,* **38**(4), 319–322.

Xiao, J. & Flandrin, P., 2007. Multitaper time-frequency reassignment for nonstationary spectrum estimation and chirp enhancement, *IEEE Trans. Signal Process.,* **55**(6), 2851–2860.

Downloaded from http://gji.oxfordjournals.org/ at Vienna University Library on April 11, 2014